

Article

Integration of Concentration-Area Fractal Modeling and Spectral Angle Mapper for Ferric Iron Alteration Mapping and Uranium Exploration in the Xiemisitan Area, NW China

Jun-Ting Qiu ¹, Chuan Zhang ^{1,*} and Xiao Hu ²

¹ National Key Laboratory of Science and Technology on Remote Sensing Information and Image Analysis, Beijing Research Institute of Uranium Geology, Beijing 100029, China;

E-Mail: qiu junting@cugb.edu.cn

² Chengdu Center of Hydrogeology and Engineering Geology, Chengdu 610081, China;

E-Mail: cughx@163.com

* Author to whom correspondence should be addressed; E-Mail: chuanzi521@163.com;

Tel.: +86-010-6496-7331; Fax: +86-010-8483-2992.

Academic Editors: James Jin-King Liu, Yu-Chang Chan, Ioannis Gitas and Prasad S. Thenkabail

Received: 3 July 2015 / Accepted: 7 October 2015 / Published: 22 October 2015

Abstract: The high-grade uranium deposits in the Xiemisitan area, northwestern China, are genetically associated with the faulting of felsic volcanic or sub-volcanic rocks. Ferric iron alteration indicates that oxidizing hydrothermal fluids percolated through the rocks. In this study, we measured the gamma-ray intensities of rocks in the Xiemisitan area and we propose a hybrid method for the mapping of ferric iron alteration using concentration-area fractal modeling and spectral angle mapper. The method enables ferric iron alteration to be distinguished from potash-feldspar granitic rocks. The mapping results were integrated with structural data to assist with exploration for uranium in the study area. Using this approach, six prospective areas of mineralization were proposed. Of these areas, two anomalies with high gamma-ray intensities of 104 and 650 U γ were identified and verified by field inspection. These observations suggest that Enhanced Thematic Mapper Plus images are a valuable tool that can improve the efficiency of uranium exploration.

Keywords: enhanced thematic mapper plus; concentration-area fractal modeling; spectral angle mapper; uranium exploration; Xiemisitan area; Northwest China

1. Introduction

Uranium is an important natural resource that is used in civilian and military industries. It is an incompatible element that becomes enriched in magma during the course of magmatic differentiation [1,2]. Hence, felsic magma usually has a high uranium content and crystallized felsic igneous rocks can host uranium mineralization [3]. The solubility of uranium depends on its valence (hexavalent uranium is more soluble in water-rich fluids than tetravalent uranium) [4,5], which is controlled mainly by the redox state of the geological environment [6]. The redox state of terrestrial igneous rocks is usually close to the fayalite-magnetite-quartz (FMQ) [7,8] buffer. Under these conditions, uranium in magma is not oxidized from the tetravalent to the hexavalent state [6], thus preventing uranium from partitioning into a water-rich magmatic volatile phase that ultimately generates economic ore bodies [9–11]. Fortunately, oxidizing surface waters percolating along geological faults or fractures can mix with post-magmatic hydrothermal solutions, resulting in a more oxidizing fluid that is capable of leaching uranium from volcanic or sub-volcanic rocks. Subsequently, precipitation from this fluid results in secondary uranium enrichment [12]. Because the oxidation state of the fluid is higher than the hematite-magnetite (HM) buffer, minerals containing ferric iron (e.g., limonite and hematite) are formed during water-rock interaction. Ferric iron alteration is observed in many volcanogenic uranium deposits in northwestern China.

Ferric iron alteration, felsic igneous rocks, and faulting are genetically related to uranium mineralization. Hence, these geological features are employed as criteria for uranium prospecting. Traditional exploration based on field survey is commonly inefficient and impractical because some regions, such as mountainous areas or the Gobi Desert in northwestern China, are inaccessible. In contrast, remote sensing technology employing low spatial and/or spectral resolution enables the rapid and low-cost collection of data from inaccessible regions, thus providing an alternative method to surveying for uranium resources.

The Enhanced Thematic Mapper Plus (ETM+) is a satellite instrument that gathers multi-spectral remote sensing data free of charge, and these data are widely used in geological studies [13,14]. Previous studies have proposed several methods and algorithms to identify alteration and lithology using the ETM+ [15–19]. In particular, the Spectral Angle Mapper (SAM) is convenient and effective because the spectra used for identification is easily acquired from spectral libraries, Analytical Spectral Devices (ASD) spectrometer measurements, or from specified pixels in remote sensing images [20]. However, the identification of hydrothermal alteration and lithology using SAM is strongly dependent on the selection of the maximum angle.

The concentration-area (C-A) fractal model proposed by Cheng *et al.* (1994) [21] can be used to compute quantitative geochemical and geophysical anomaly thresholds, and it has been widely used in geological, geochemical, and geophysical exploration [22–32]. Combining the C-A fractal model with the Crosta technique has been shown to be effective in identifying alteration zones in the Hashtjin area (Iran) [33], which suggests that the C-A fractal model is also useful for remote sensing studies. However, the Crosta technique may be sensitive to the presence of red potash–feldspar granitic rocks. Hence, this combined method may be unsuitable for the mapping of ferric iron alteration when such granitic rocks are present in the study area.

In this paper, we propose a hybrid method for alteration mapping that uses the C-A fractal model to determine the maximum angle of SAM. We present a detailed description of data processing for the

mapping of ferric iron alteration in the Xiemisitan area of northwestern China. The mapping result was confirmed by field inspection and was integrated with lithological and structural information to assist in exploration for uranium in the study area.

2. Geological Setting

The Xiemisitan area (46°45'–46°25'N; 84°50'–85°50'E), located west of the Junggar Basin in northwestern China (Figure 1a), contains the E–W running Xiemisitan mountain range at its center (Figure 1b). The mountain range is composed primarily of Devonian to Carboniferous volcanic and sub-volcanic rocks (including basalt, andesite, rhyolite, quartz porphyry, granite porphyry, and ignimbrite) and subordinate amounts of sedimentary rock (including carbonate, sandstone, and conglomerate) [34]. Locally these rocks have been intruded by Hercynian magmatic rocks (including gabbro, diabase, diorite, monzogranite, and granite) and are cross-cut and bounded by the regional NE-trending Mengbulake Fault and the E–W-trending Bayinbulake Fault. Local faults and fractures are well-developed in the Xiemisitan area and are generally oriented NNE–SSW, NE–SW, and NW–SE.

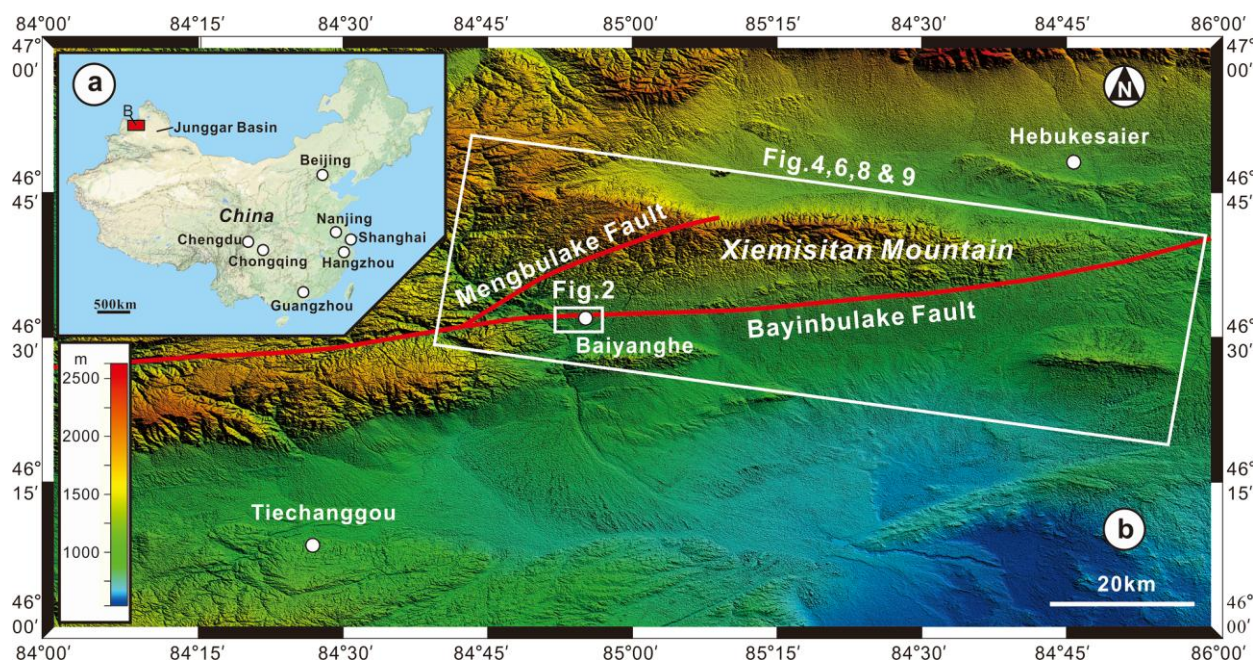


Figure 1. (a) Location of the Xiemisitan area in NW China. (b) Elevation map derived from ASTER illustrating the physiography of the Xiemisitan area.

2.1. Geology of Baiyanghe Uranium Deposit

The Baiyanghe uranium deposit in the Xiemisitan area (Figure 2) has a typical volcanogenic origin [35,36]. The deposit is hosted by the Yangzhuang stock, which consists mainly of potash–feldspar granite porphyry and minor quartz porphyry. The weighted mean laser ablation-inductively coupled plasma-mass spectrometry (LA-ICP-MS) U–Pb zircon age of the granite porphyry is 313.4 ± 2.3 Ma [34]. The stock was emplaced into Devonian intermediate-acid volcanic and pyroclastic rocks, resulting in a friable and altered contact zone. The alteration minerals include hematite,

limonite, fluorite, and chlorite. The deposit is located proximal to the E–W-trending Bayinbulake Fault (Figure 1b). The joints in the footwall of the fault can be divided into two groups. The first group is truncated by the second group (Figure 3a), suggesting that the direction of maximum stress changed in a manner that caused the fault style to change from reverse faulting to normal faulting. Some fractures (Figure 3b) in the porphyry stock are parallel to the Bayinbulake Fault and may have formed during the transition from compression to extension.

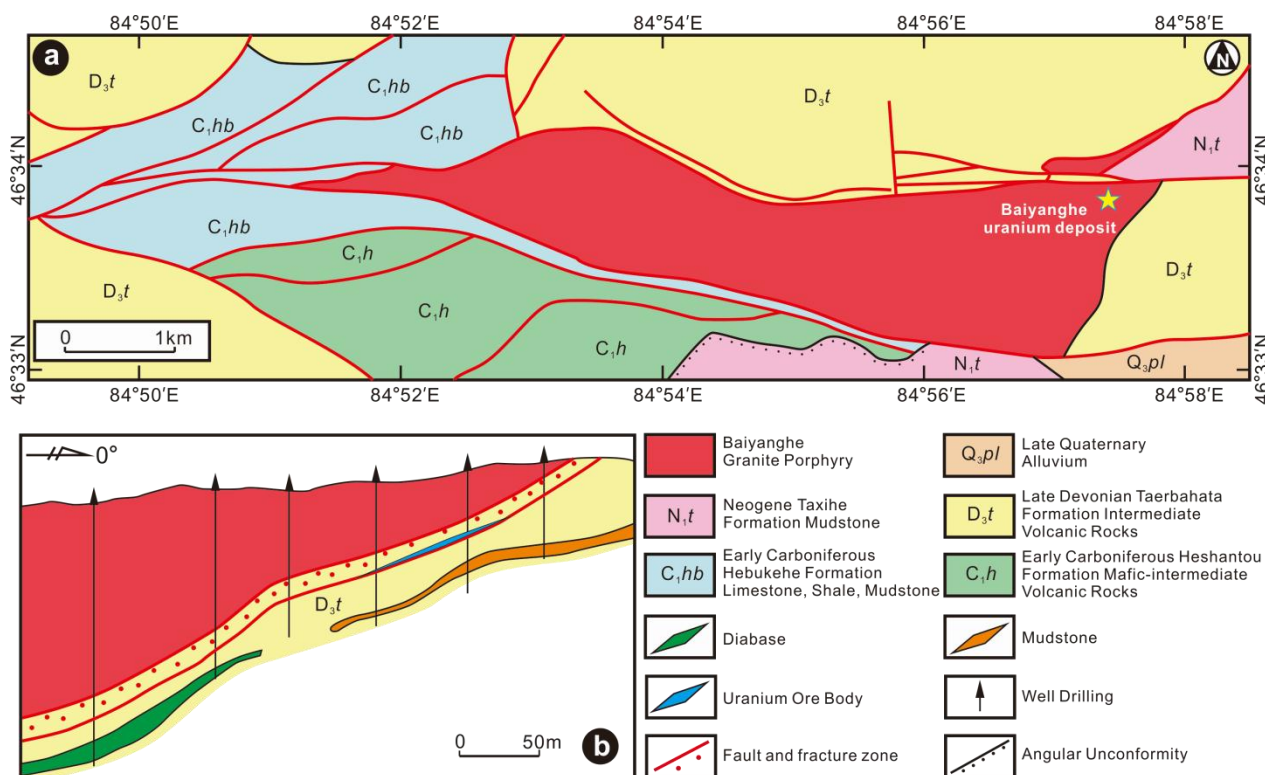


Figure 2. (a) Geological map of the Baiyanghe Uranium deposit. (b) Geological profile shows that uranium ore bodies are distributed along the fracture zone between granite porphyry and the Taerbahata formation (modified after [36]).

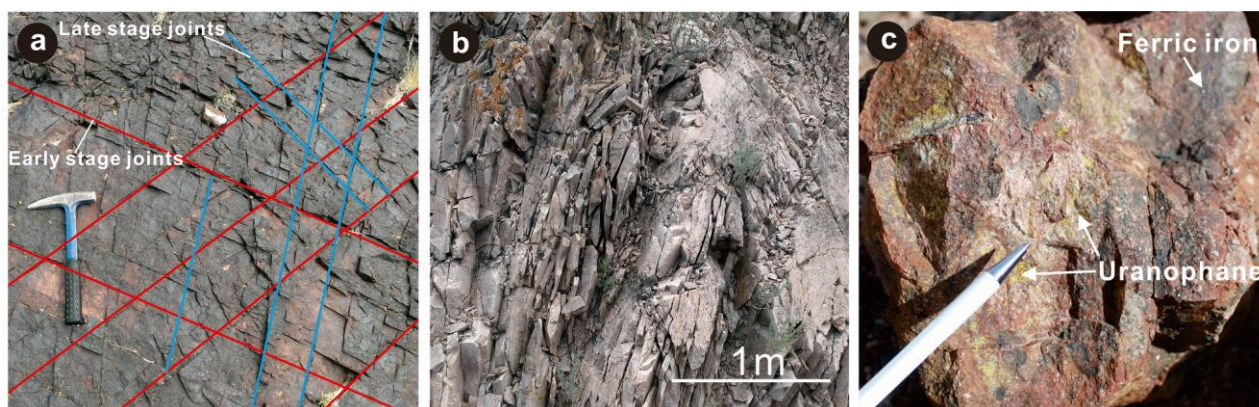


Figure 3. (a) Two groups of joints, in which the second group is limited by the first group. (b) Penetrative fractures in the porphyry stock. (c) Uranium mineralization is associated with ferric iron alteration.

2.2. Ore Minerals in Baiyanghe Uranium Deposit

Ore minerals in the Baiyanghe uranium deposit include pitchblende and uranophane. Pitchblende is scattered and generally associated with fluorite veins lining small fractures or within the groundmass of felsic rocks, whereas uranophane mainly occurs on the surface of some felsic rocks with ferric iron alteration (Figure 3c). The U-Pb isotopic ages for the pitchblende can be divided into four stages, including 237.8–224 Ma, 197.8 Ma, 97.8Ma, and 30 Ma [36], suggesting post-magmatic and multi-stage mineralization of pitchblende. Because the REE patterns of pitchblende ore are similar to those of the granite porphyry, the granite porphyry may be the source of uranium in the Baiyanghe deposit that was further enriched through later hydrothermal activity [36].

2.3. Fluid Inclusions in Baiyanghe Uranium Deposit

Fluid inclusions in pitchblende-associated fluorites have homogenization temperatures of 90 °C–372 °C and salinities of 1.49%–19.72% [36–39]. The carbon ($\delta^{13}\text{C}_{\text{PDB}}$) and oxygen ($\delta^{16}\text{O}_{\text{SMOW}}$) isotope ratios range from –4.9‰ to –10.9‰ and from 14.4‰ to 21.6‰, respectively [36–39], suggesting that the ore-forming fluids originated from multiple sources, including metamorphic and meteoric waters. The occurrence of ferric iron alteration indicates that the fluids were oxidized above the HM buffer.

3. Methodology

As described in Section 1, SAM is a convenient and effective method for alteration mapping but its result is strongly dependent on maximum angle selection. The C-A fractal model, which permits anomaly thresholds to be quantitatively computed, provides an approach to determine the maximum angle of SAM. For a better understanding, the two methods are briefly described as follows.

3.1. Spectral Angle Mapper

The SAM algorithm calculates the spectral similarity between the image and reference spectra by treating them as vectors in n-dimensional space and computing the corresponding angle between them [32]. The result is not affected by solar illumination factors because the angle between the two vectors is independent of vector length [32]. In this study, we use the cosine value of the spectral angle to represent the degree of similarity between the image and reference spectra. High cosine values between the two spectra indicate high similarity, whereas low values indicate low similarity. The cosine value can be computed using Equation (1), where nb is the number of bands, t_i is the reflectance of band i of the image spectrum, and r_i is the reflectance of band i of the reference spectrum.

$$\cos\alpha = \frac{\sum_{i=1}^{\text{nb}} t_i r_i}{\sqrt{\sum_{i=1}^{\text{nb}} t_i^2} \sqrt{\sum_{i=1}^{\text{nb}} r_i^2}} \quad (1)$$

3.2. Concentration-Area Fractal Model

The C-A fractal model proposed by Cheng *et al.* (1994) [21] can be used to separate geochemical and geophysical anomalies from background values in order to characterize the distribution of elements in a

study area. The general form of the model is shown in Equation (2), where $A(\rho)$ denotes the area with concentration values greater than the contour value ρ , v represents the threshold, and a_1 and a_2 are characteristic exponents. The area $A(\rho)$ for a specified ρ is equal to the cell area multiplied by the number of cells with pixel values greater than ρ . The changes in slope between straight-line segments on a log–log plot and the corresponding values of ρ are used as cut-off (threshold) values to separate pixel values into components that represent different causal factors. In this study, we use the C-A fractal model to separate pixels with different cosine values and to determine the threshold value between different populations.

$$A(\rho \leq v) \propto \rho^{-a_1}; A(\rho \geq v) \propto \rho^{-a_2} \quad (2)$$

4. Experiments

This section presents a detailed description of data acquisition, processing, and modeling procedures for the mapping of ferric iron alteration in the study area.

4.1. Reference Spectrum of Ferric Iron

Ferric iron alteration is genetically associated with uranium mineralization and is therefore a valuable pathfinder for uranium exploration. Because of the low spatial resolution of ETM+ images and the possibility of mixed pixel effects, the spectrum of a ferric iron-bearing rock, rather than the spectra of pure ferric iron-bearing minerals, was measured in this study.

The rock sample used for spectrum determination was collected from the Baiyanghe deposit. It is a granitic rock that contains uranophane and experienced hydrothermal alteration. Ferric iron bearing minerals can be observed on the surface of the sample. Some feldspars have altered to clay minerals. The measurement was carried out using an ASD Fieldspec Pro spectrometer at National Key Laboratory of Science and Technology on Remote Sensing Information and Image Analysis. The spectral range of the instrument is 350 to 2500 nm. The spectral resolution is 3 nm between 350 and 1000 nm, and 10 nm between 1000 and 2500 nm. The instrument was set up according to the manufacturer's instructions described in the Labspec4 user manual. An accessory light source was employed to measure spectra in lieu of sunlight. During the measurement, a relatively flat rock surface containing ferric iron alteration was chosen to avoid potential interference from background environmental fluorescence. A white reference light was introduced during the measurement procedure to optimize and calibrate the instrument. Five spectra of the rock sample were measured and recorded using the RS³ software. The data were converted into ASCII file format using ViewSpecPro software (see Supplementary Table 1).

The spectra listed in Supplementary Table 1 was converted to Spectral Library File using Spectral Library Builder function of ENVI 5.0 software, and then resampled to Landsat TM7 sensor spectra with Spectral Library Resampling function. The reflectance values of resampled spectra and their average values, *i.e.* the reflectance values of the reference spectrum (used to compute cosine values of spectral angles) are listed in Table 1.

4.2. Processing of ETM+ Image

The original ETM+ image of the study area was acquired during the dry season on 27 June 2000 by the Landsat 7 satellite (Path = 145, Row = 28) and processed to generate a standard product by the United

States Geological Survey (USGS) on 22 February 2008. The USGS product was downloaded from the Earth Explorer platform (www.earthexplorer.usgs.gov). It contains one panchromatic band (band 8) and seven multi-spectral bands (bands 1–7). The spatial resolution of band 8 is 15 m and the resolutions of the multi-spectral bands are 30 m except for band 6 (60 m). The cloud content of the product is less than 1%. Band 6 was excluded from the image dataset because it is a thermal infrared band that may be influenced by temperature variations related to elevation changes.

Table 1. Reflectance values of resampled spectra and their average values.

ETM+Band	Reflectance of Resampled Spectra					Average	
	RS1	RS2	RS3	RS4	RS5	Value *	r _i **
1	0.103775	0.102896	0.102278	0.102006	0.101557	0.102502	r ₁
2	0.150469	0.14923	0.148155	0.147519	0.146886	0.148452	r ₂
3	0.204367	0.202621	0.201106	0.200175	0.199321	0.201518	r ₃
4	0.23347	0.231416	0.229618	0.228519	0.227543	0.230113	r ₄
5	0.310907	0.308077	0.305459	0.303935	0.302502	0.306176	r ₅
7	0.261233	0.258663	0.256412	0.255086	0.253856	0.25705	r ₆

* The average values were calculated from the reflectance of resampled spectra (RS1 to RS5) and will be used to compute cosine values of spectral angles. ** r_i is the reflectance of No. i band of reference spectrum (See Equation (1)).

The ETM+ image was oriented to acquire part of the Xiemisitan area and was then calibrated using the “Landsat Calibration” function in ENVI 5.0 software. An atmosphere correction was carried out using the “Quick Atmosphere Correction” function. Since pixel values in the calibrated and corrected image were multiplied by a constant to return integer values by ENVI software after atmosphere correction, the image was normalized using the “Band Math” function by dividing by 10,000.

The normalized ETM+ image and the reference spectrum listed in Table 1 were used to compute the cosine values of spectral angles using the “Band Math” function following the method described in Section 3.1. The computation expression is provided in Supplementary 1 and the result is shown in Figure 4.

4.3. C-A Fractal Modeling

In this study, the cell area (*i.e.*, one pixel) is 30 × 30 m and the total number of cells in the cosine image (Figure 4) is 5.031 × 10⁶. The contour value ρ denotes the pixel value in the cosine image, and it ranges from 0.6723 to 0.9993.

The “Density Slice” function in ENVI 5.0 software was used to divide the cosine map into 3270 gray levels each of which displays a variation of ~0.0001 in the cosine value. The density slice image was saved as a “Class Image” for statistical analysis, using the “Class Statistic” function. The results (Supplementary Table 2) were exported to Microsoft Excel 2007 to create a histogram (Figure 5a) and log–log plots (Figure 5b).

5. Results

The mapping result of ferric iron alterations for the study area using the hybrid method of SAM and C-A fractal model is presented in this section. Additionally, we determined the gamma intensities of rocks in the Xiemisitan area for further uranium exploration application.

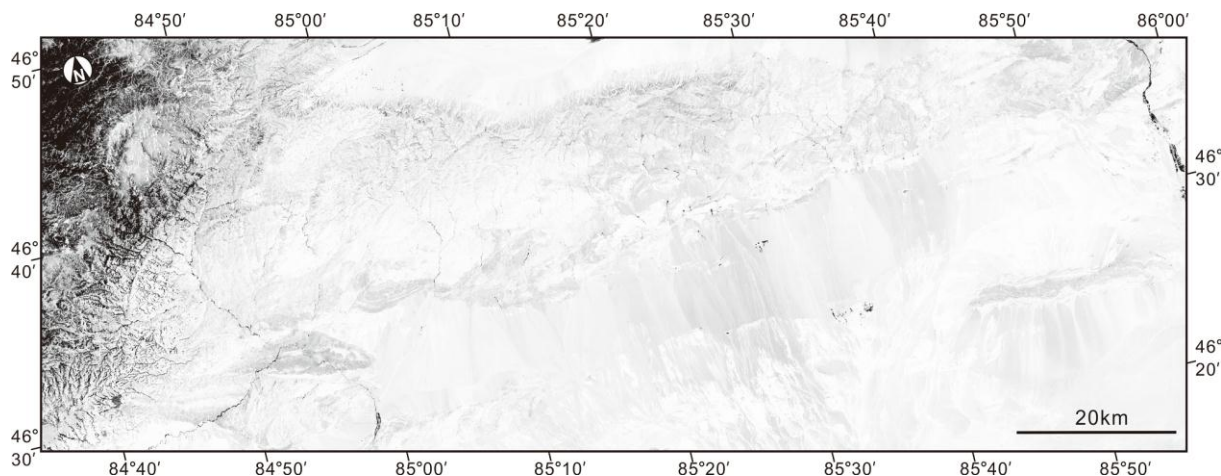


Figure 4. Map of cosine values of spectral angles between image and reference spectra. The image spectra were obtained from the pro-processed ETM+ image, and the reflectance values of reference spectrum are listed in Table 1.

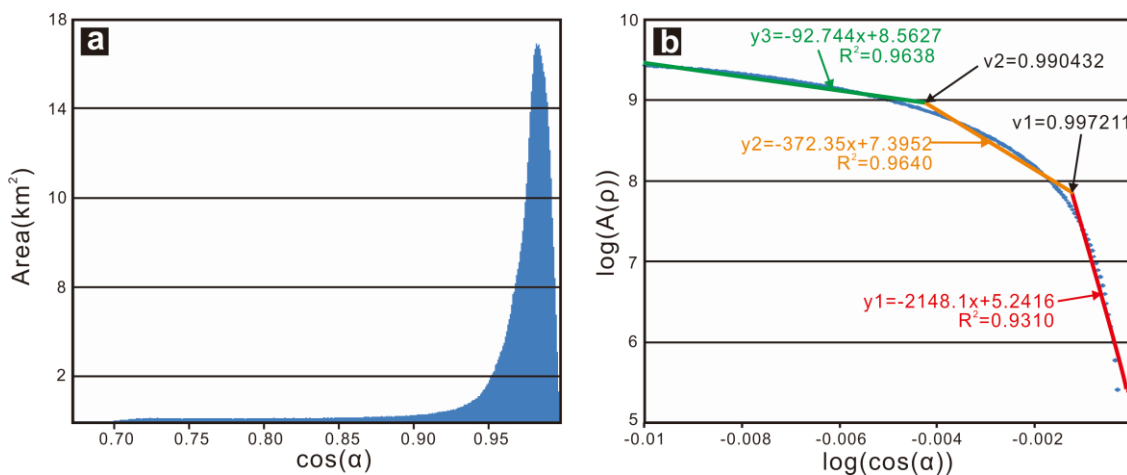


Figure 5. (a) Histogram graph of area *versus* $\cos(\alpha)$ in the Xiemisitan area. (b) Log–log plot of $A(\rho)$ *versus* $\cos(\alpha)$ in the Xiemisitan area. The straight lines shown in Figure 5b were fitted using least square method.

5.1. Ferric Iron Alteration Mapping

Generally, the mapping results for iron oxides can be classified into the background, low intensity, and high intensity areas [33]. We, therefore, identified three populations of data based on the log–log graph shown in Figure 5b. Three linear segments were fitted to the data using the least squares method. The cut-off (threshold) value was determined from the x-coordinate of the intercept between two adjoining line segments, at which the product of the linear correlation coefficients is a maximum. The

calculated values for thresholds v_1 and v_2 (Figure 5b) are 0.9972 and 0.9904, respectively. These thresholds were used to divide the map of cosine values into a red area where pixel values are greater than 0.9972, and a yellow area where pixel values range from 0.9904 to 0.9972 (Figure 6).

A belt of ferric iron alteration along the contact zone between the porphyry stock and the Devonian intermediate volcanic rocks (north of the Baiyanghe uranium deposit) offers a good opportunity to test the mapping results. The E–W trending belt is ~4 km long and 25–45 m wide, and consists mainly of potash–feldspar granite porphyry that contains ferric-iron-bearing minerals (e.g., limonite and hematite) and minerals indicative of argillic alteration. As shown in Figure 6, the mapping results for ferric iron alteration can be divided into two groups. The first group contains pixels with high cosine values (red pixels in Figure 6) that are similar to the reference spectrum of ferric iron alteration. This group is spatially consistent with the area where ferric iron minerals are abundant. In contrast, the second group contains pixels with low cosine values (yellow pixels in Figure 6) that are markedly different to the reference spectrum, consistent with their location in areas with minor or no ferric-iron-bearing minerals. The distribution of the second group of yellow pixels coincides with the distribution of potash–feldspar porphyry in some places (Figure 7, also see Supplementary 2). Collectively, these observations suggest that the combination of SAM and the C-A fractal model is not only useful for the mapping of ferric iron alteration, but also for distinguishing between ferric iron alteration and potash–feldspar porphyry rocks, which are both genetically related to uranium mineralization in the Baiyanghe deposit. Hence, the mapping results will be valuable for uranium exploration in the Xiemisitan area.

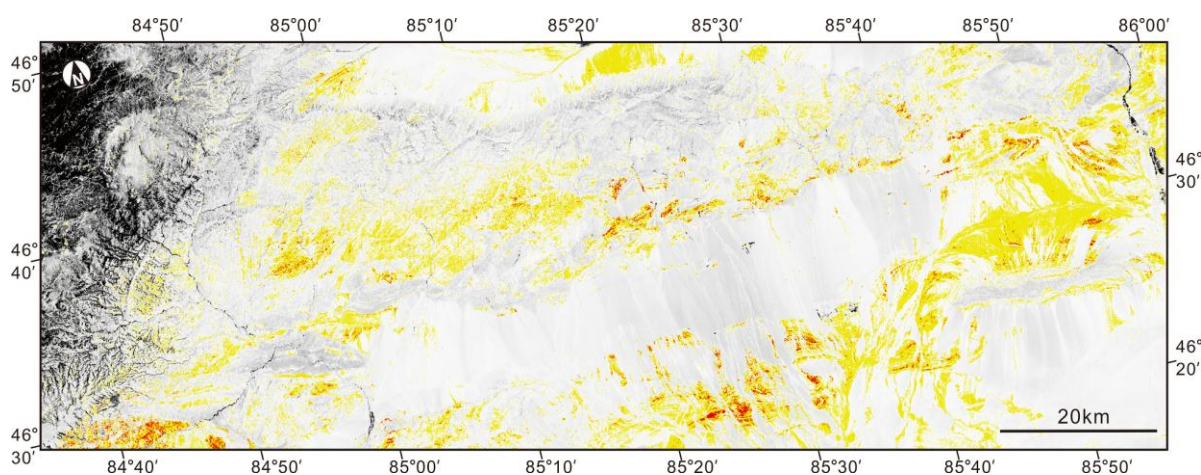


Figure 6. Distribution of ferric iron bearing rocks mapped by combination method of SAM and C-A fractal model. Cells in red area have pixel values greater than 0.9972 and those in yellow area have pixel values in the range of 0.9904 to 0.9972.

5.2. Gamma Intensities of Rocks

Measuring the gamma-ray intensities of rocks is an effective approach to identifying rocks that are enriched in uranium. In this study, 500 magmatic and sedimentary rock samples were collected from the Xiemisitan area. In addition, ferric iron-bearing rocks from the Baiyanghe uranium deposit were collected. The gamma-ray intensities of these rocks were measured using an HD-2000 gamma indicator developed by the Beijing Research Institute of Uranium Geology, Beijing, China. The intensity unit is $U\gamma$. Please refer to Supplementary 3 or www.bjhdkj.com for more information about the indicator.

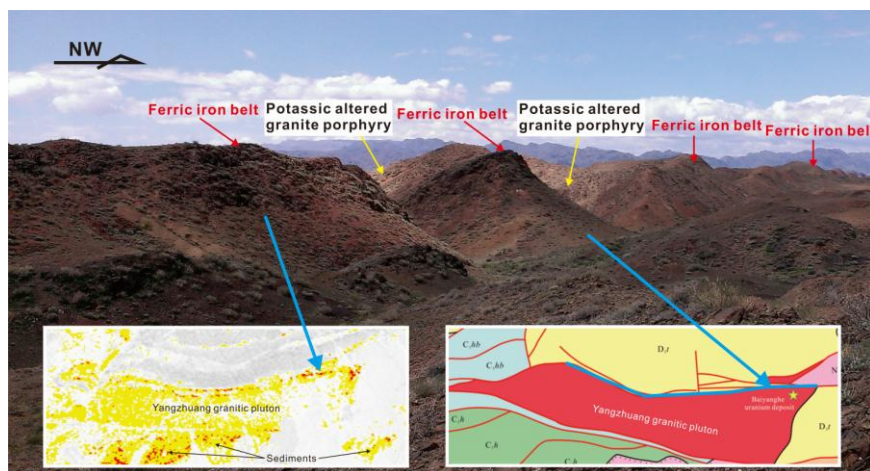


Figure 7. Photograph of ferric iron alteration belts in the north of the Baiyanghe uranium deposit.

The gamma-ray intensities of felsic magmatic and volcanic rocks (35 to 42 U γ) in the Xiemisitan area are higher than those of andesitic (22 to 29 U γ) and mafic rocks (17 to 20 U γ), which is expected because of the incompatible behavior of uranium during magmatic differentiation. Sedimentary rocks, including sandstone, conglomerate, and carbonate, usually have low gamma-ray intensities of 23 to 29 U γ . The ferric iron-bearing rocks in the Baiyanghe deposit yield higher gamma-ray intensities (mean of 67 U γ), and rocks containing uranophane yield even higher gamma-ray intensities (mean of 953 U γ ; Table 2). Previous studies reported uranium contents of 13.43 ppm, 101.09 ppm (~0.01%), and ~1265.58 ppm (0.13%) for felsic magmatic rocks, ferric iron rocks with no uranophane, and ferric iron rocks with uranophane, respectively [40]. Since the anomaly threshold of uranium is 0.01% (67 U γ in this study) in China, we use 67 U γ as the cut-off value to distinguish uranium anomaly from background.

Table 2. Gamma intensities for different rocks in the Xiemisitan area.

Class	Rock Type	Gamma Intensity *
Felsic	rhyolite	35 ± 9 (n = 32)
	Quartz porphyry	39 ± 12 (n = 15)
	Granite porphyry	42 ± 11 (n = 110)
	Monzogranite	38 ± 12 (n = 20)
	Granite	37 ± 14 (n = 25)
Intermediate	Andesite	22 ± 7 (n = 40)
	Diorite	27 ± 10 (n = 40)
	Ignimbrite	29 ± 12 (n = 20)
Mafic	Basalt	17 ± 3 (n = 10)
	Diabase	19 ± 5 (n = 20)
	Gabbro	20 ± 7 (n = 10)
Sedimentary	Sandstone	29 ± 12 (n = 50)
	Conglomerate	27 ± 10 (n = 20)
	Carbonate rock	23 ± 7 (n = 50)
Ferric iron rocks	Ferric iron rocks with no uranophane	67 ± 31 (n = 25)
	Ferric iron rocks with uranophane	953 ± 611 (n = 7)

* Gamma intensities were measured by HD-2000 gamma indicator developed by Beijing Research Institute of Uranium Geology; Errors are 2 σ ; The unit is U γ .

6. Discussion

In this section, we first discuss the advantages of the hybrid method of SAM and C-A fractal model, then integrate mapping results with structural data to assist with exploration for uranium in the study area.

6.1. Advantages of the Method

The C-A fractal model can be used to identify different data populations for image display and to determine the threshold values that separate each population. It is useful not only for geochemical and geophysical studies but also for remote sensing because the model generates different populations of pixel values and takes into account the spatial and geometrical properties of real-world ground features [33]. The SAM method enables rapid mapping and suppresses the influence of shading effects to accentuate the reflectance characteristics of the target [20]. In addition, the reference spectrum used for SAM mapping is easy to obtain.

Previous studies proposed that the C-A fractal model could be combined with the Crosta technique to map ferric iron alteration [31–33]. However, this method may be compromised by the red color of potash–feldspar granitic rocks, which causes high reflectance values in band 3 and low values in band 1 that are similar to those of ferric-iron-bearing minerals. The method presented in this study, which combines SAM and the C-A fractal model, enables a more robust identification of ferric iron alteration because it uses a greater number of spectral characteristics. As shown in Figure 6, the method can distinguish ferric iron alteration from potash–feldspar granite porphyry. The method can potentially also be used for mapping other types of hydrothermal alteration using appropriate reference spectra. The whole data processing procedure can be completed using the ENVI 5.0 and Microsoft Excel software packages without additional programming.

6.2. Application to Uranium Exploration

Faults and fractures play an important role in fluid migration and uranium mineralization. These structures can be identified by processing a ETM+ image to clearly show changes in rocks units caused by displacement and deformation [41]. In this study, structural separation was identified through the interpretation of ETM+ images using a band combination (Red = band 4; Green = band 3; Blue = band 1) and was based on evidence such as vegetation change, the deviation of stream paths, and abrupt lithology changes as depicted by changes in the tones and textures of images. The result is shown in Figure 8.

The faults identified with this method and the maps of ferric iron alteration and potash–feldspar granite were used for uranium exploration in the Xiemisitan area. Six prospective areas of uranium mineralization were recognized and selected for measurement of gamma-ray intensity. These areas are denoted by the numbers in Figure 9.

The radioactive element content of each area was inferred from the gamma-ray intensity measured using the HD-2000 gamma indicator. Two gamma-ray anomalies from area 5 were identified and had gamma-ray intensities much higher than those of felsic rocks (35 to 42 $U\gamma$) in the Xiemisitan area (as described in Section 2.3). The first anomaly had a gamma-ray intensity of 104 $U\gamma$ and was found in fractures in a granite porphyry stock (Figure 10a) where ferric iron alteration and faults are well developed. The second

anomaly was also found in granite porphyry affected by ferric iron alteration (Figure 10b) and is characterized by a gamma-ray intensity of 650 U γ . The two newly discovered anomalies suggest that ETM+ images are valuable for uranium exploration.

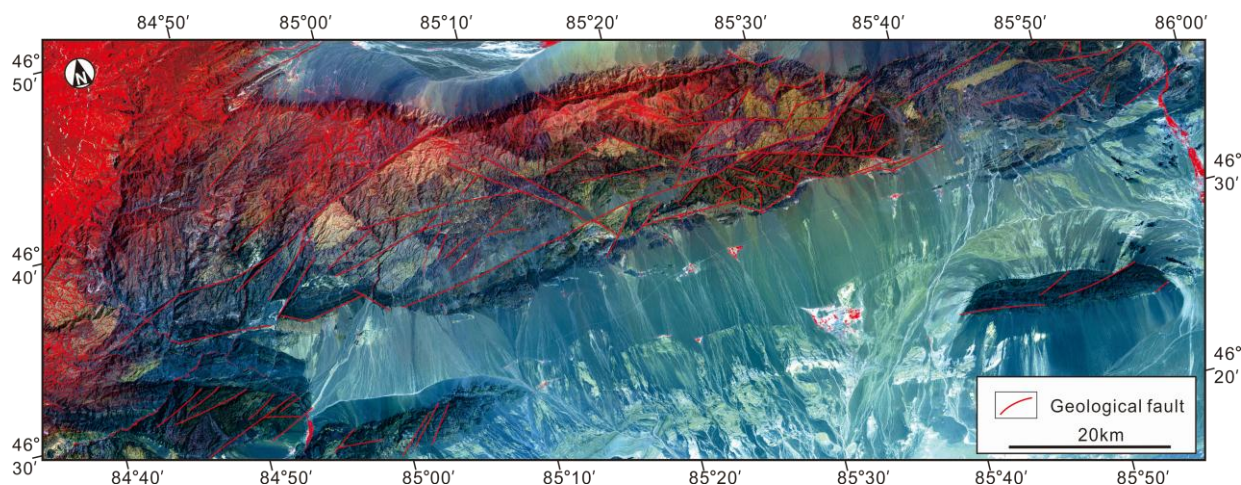


Figure 8. Linear Structural interpretation result for the Xiemisitan area (R:G:B = 4:3:1).

Although two anomalies were recognized in area 5, other areas show no apparent gamma-ray anomalies despite the occurrence of ferric iron alteration. This apparent discrepancy can be attributed to the surface oxidation of felsic rocks containing iron-bearing minerals. For example, ferric iron alteration is well developed on the surface of the granite porphyry in area 6, but does not occur within the fresh interior of the rock (Figure 11). In this case, the ferric iron alteration was related to surface oxidation rather than interaction with hydrothermal fluids. The gamma-ray intensities of the granite porphyry range from 35 to 47 U γ , suggesting no uranium enrichment in this area.

The surface oxidation of iron means that the efficiency of uranium exploration using ETM+ images alone is severely limited because false uranium prospects will be identified. Fortunately, uranium-bearing ferric iron alteration is usually characterized by higher gamma-ray intensity (sometimes by one order of magnitude) than uranium-barren rocks. Hence, airborne gamma-ray measurements are a useful tool for uranium prospecting.

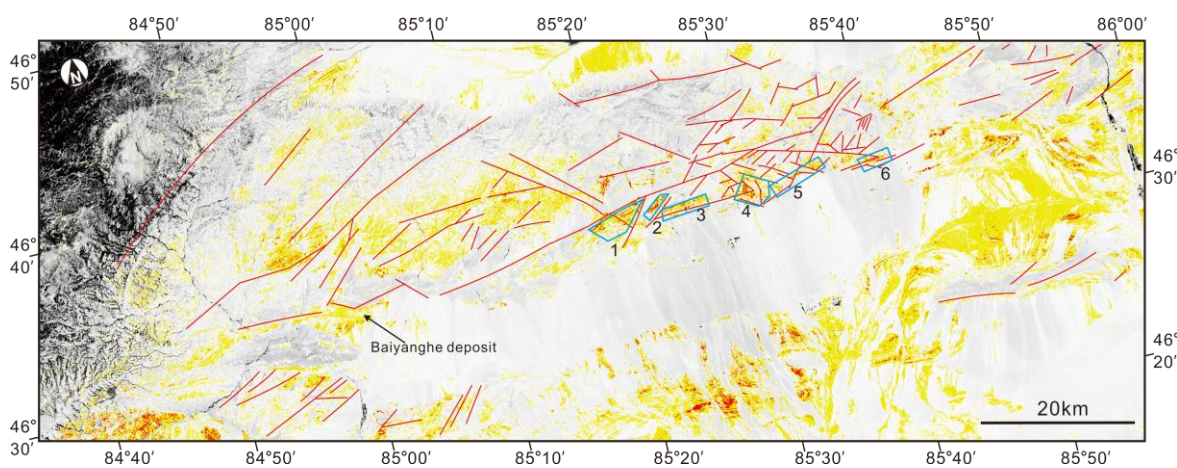


Figure 9. Distribution of uranium prospects (red pixels represent ferric iron, while yellow pixels represent felsic magmatic rocks).

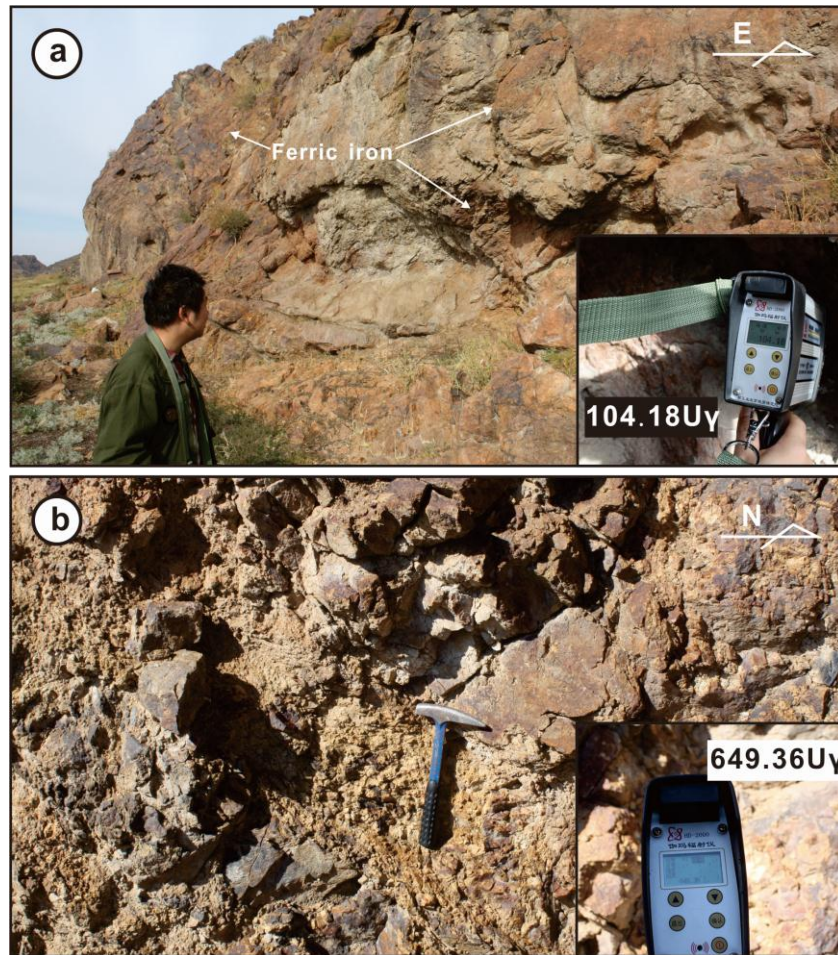


Figure 10. (a & b) Two radioactive anomalies (Gamma intensities were measure by HD-2000 gamma indicator developed by Beijing Research Institute of Uranium Geology). High quality photographs can be found in Supplementary 4–7.



Figure 11. Ferric iron is well developed on the surface of the granite porphyry, but does not occur in the fresh part of the rock in area 6.

Since ETM+ images are freely available and easy to acquire and process, we propose a two-stage procedure for uranium exploration. The ETM+ image is used in the first stage to identify possible

uranium-enriched areas based on regional lithology, ferric iron alteration mapping, and the presence of faults. In the second stage, these areas are further evaluated by airborne gamma-ray spectrometer or ground-based gamma-ray measurements to identify areas of high intensity.

7. Conclusions

The gamma-ray intensity of rocks is important for uranium exploration. The gamma-ray intensities for the felsic, intermediate, mafic, and sedimentary rocks in the Xiemisitan area are 35–42, 22–29, 17–20, and 23–29 $U\gamma$, respectively. Rocks containing uranium-bearing ferric iron alteration have gamma intensities of about one order of magnitude (953 $U\gamma$) higher than those of uranium-barren rocks. Hence, high gamma-ray intensities can be used as a pathfinder for uranium exploration in the Xiemisitan area.

A previous method combined the C-A fractal model with the Crosta technique to map ferric iron alteration, but this method is compromised when potash–feldspar granitic rocks are present in the study area. In contrast, the hybrid method of SAM and the C-A fractal model presented in this study uses a greater number of spectral characteristics and thus can robustly distinguish ferric iron alteration from potash–feldspar granite porphyry. Because the reference spectrum is easy to obtain, the hybrid method can potentially be used to map other types of hydrothermal alteration using appropriate reference spectra. In addition, the processing procedure can be conveniently completed using the ENVI 5.0 and Microsoft Excel software packages without additional programming.

The case study reported here demonstrates that ETM+ images can be used to identify ferric iron alteration, potash–feldspar granitic rocks, and geological faults. Hence, ETM+ images are valuable during the early stages of uranium exploration. However, it was also found that the surface oxidation of felsic rocks containing iron-bearing minerals might limit the efficiency of uranium prospecting. Therefore, validation of prospective areas of mineralization using airborne or ground-based gamma-ray measurements is essential for efficient uranium exploration using ETM+ images.

Acknowledgments

This study was financially supported by the foundation (No. 1212011220277) of China Geological Survey, Foundation of CNNC (No. YLCD116-4), and the Youth Foundation of BRIUG (No. DD1405-A). Thanks are due to the editors for their editorial handling and five anonymous reviewers for their comments and suggestions.

Author Contributions

Jun-Ting Qiu wrote this paper and did the field work; Chuan Zhang measured gamma intensities of rocks and determined spectra of ferric iron bearing rocks. Xiao Hu did the C-A fractal modeling and alteration mapping.

Conflicts of Interest

The authors declare no conflict of interest.

References

1. Henderson, P. *Inorganic geochemistry*; Pergamon Press: Oxford, UK, 1982.
2. Keppler, H.; Wyllie, P.J. Partitioning of Cu, Sn, Mo, W, U, and Th between melt and aqueous fluid in the systems haplogranite-H₂O-HCl and haplogranite-H₂O-HF. *Contrib. Mineral. Petrol.* **1991**, *109*, 139–150.
3. Ling, H.F. Origin of hydrothermal fluids of granite-type uranium deposits: Constraints from redox conditions. *Geol. Rev.* **2011**, *57*, 193–206. (In Chinese)
4. Schreyer, J.M.; Baes, C.F., Jr. The solubility of uranium (VI) orthophosphates in phosphoric acid Solutions. *J. Am. Chem. Soc.* **1954**, *76*, 354–357.
5. Ryan, J.L.; Rai, D. The solubility of uranium (IV) hydrous oxide in sodium hydroxide solutions under reducing conditions. *Polyhedron* **1987**, *2*, 947–952.
6. Shock, E.L.; Sassani, D.C.; Betz, H. Uranium in geologic fluids: estimates of standard partial molal properties. oxidation potentials, and hydrolysis constants at high temperatures and pressures. *Geochim. et Cosmochim. Acta* **1997**, *61*, 4245–4266.
7. Drake, M.J. The oxidation state of europium as indicator of oxygen fugacity. *Geochim. et Cosmochim. Acta* **1975**, *39*, 55–64.
8. Scaillet, B.; Evans, B.W. The 15 June 1991 Eruption of Mount Pinatubo. I. Phase Equilibria and Pre-eruption P–T–fO₂–fH₂O Conditions of the Dacite Magma. *J. Petrol.* **1999**, *40*, 381–411.
9. Candela P.A.; Holland H.D. A mass-transfer model for copper and molybdenum in magmatic hydrothermal systems—The origin of porphyry-type ore-deposits. *Econ. Geol.* **1986**, *81*, 1–19.
10. Candela, P.A.; Bouton, S.L. The influence of oxygen fugacity on tungsten and molybdenum partitioning between silicate melts and ilmenite. *Econ. Geol.* **1990**, *85*, 633–640.
11. Lynton, S.J.; Candela, P.A.; Piccoli, P.M. An experimental-study of the partitioning of copper between pyrrhotite and a high-silica rhyolitic melt. *Econ. Geol.* **1993**, *88*, 901–915.
12. Tartèse, R.; Boulvais, P.; Poujol, M.; Gloaguen, E.; Cuney, M. Uranium mobilization from the variscan questembert syntectonic granite during fluid-rock interaction at depth. *Econ. Geol.* **2013**, *108*, 379–386.
13. Ranjbar, H.; Honarmand, M.; Moezifar, Z. Application of the Crosta technique for porphyry copper alteration mapping, using ETM+ data in the southern part of the Iranian volcanic sedimentary belt. *J. Asian Earth Sci.* **2004**, *24*, 237–243.
14. Aydal, D.; Ardal, E.; Dumanlilar, Ö. Application of the Crosta technique for alteration mapping of granitoidic rocks using ETM+ data: case study from eastern Tauride belt (SE Turkey). *Int. J. Remote Sens.* **2007**, *28*, 3895–3913.
15. Sabins, F.F. Remote sensing for mineral exploration. *Ore Geol. Rev.* **1999**, *14*, 157–183.
16. Zhao, Z.; Zhang, Y.; Cheng, Q.; Chen, J. Extraction of Mineral Alteration Zone from ETM + Data in Northwestern Yunnan, China. *J. China Univ. Geosci.* **2008**, *19*, 416–420. (In Chinese)
17. Zoheir, B.; Emam, A. Integrating geologic and satellite imagery data for highresolution mapping and gold exploration targets in the South Eastern Desert, Egypt. *J. Afr. Earth Sci.* **2012**, *66*, 22–34.
18. Ciampalini, A.; Garfagnoli, F.; Antonielli, B.; Del Ventisette, C.; Moretti, S. Photo-lithological map of the southern flank of the Tindouf Basin (Western Sahara). *J. Maps* **2012**, *8*, 453–464.

19. Ciampalini, A.; Garfagnoli, F.; Antonielli, B.; Moretti, S.; Righini, G. Remote sensing techniques using Landsat ETM+ applied to the detection of iron ore deposits in Western Africa. *Arabian J. Geosci.* **2013**, *6*, 4529–4546.
20. Kruse, F.A.; Lefkoff, A.B.; Boardman, J.W.; Heidebrecht, K.B.; Shapiro, A.T.; Barloon, P.J.; Goetz, A.F.H. The Spectral Image Processing System (SIPS)—Interactive visualization and analysis of imaging spectrometer data. *Remote Sens. Environ.* **1993**, *44*, 145–163.
21. Cheng, Q.; Agterberg, F.P.; Ballantyne, S.B. The separation of geochemical anomalies from background by fractal methods. *J. Geochem. Explor.* **1994**, *51*, 109–130.
22. Afzal, P.; Khakzad, A.; Moarefvand, P.; Rashidnejad Omran, N.; Esfandian, B.; Fadakar Alghalandis, Y. Geochemical anomaly separation by multifractal modeling in Kahang (Gor Gor) porphyry system, Central Iran. *J. Geochem. Explor.* **2010**, *104*, 34–46.
23. Agterberg, F.P.; Cheng, Q.; Brown, A.; Good, D. Multifractal modeling of fractures in the Lac du Bonnet Batholith, Manitoba. *Comput. Geosci.* **1996**, *22*, 497–507.
24. Cheng, Q. Spatial and scaling modelling for geochemical anomaly separation. *J. Geochem. Explor.* **1999**, *65*, 175–194.
25. Cheng, Q. Multifractal theory and geochemical element distribution pattern. *Earth Sci. J. China Univ. Geosci.* **2000**, *25*, 311–318. (In Chinese)
26. Goncalves, M.A.; Vairinho, M.; Oliveira, V. Study of geochemical anomalies in Mombeja area using a multifractal methodology and geostatistics. In Proceedings of International Association for Mathematical Geology Meeting, Ischia, Italy, 6–9 October 1998; pp. 590–595.
27. Hassanpour, S.; Afzal, P. Application of concentration-number (C-N) multifractal modeling for geochemical anomaly separation in Haftcheshmeh porphyry system, NW Iran. *Arab. J. Geosci.* **2013**, *6*, 957–970.
28. Sim, B.L.; Agterberg, F.P.; Beaudry, C. Determining the cutoff between background and relative base metal contamination levels using multifractal models. *Comput. Geosci.* **1999**, *25*, 1023–1042.
29. Zuo, R. Decomposing of mixed pattern of arsenic using fractal model in Gangdese belt, Tibet, China. *Appl. Geochem.* **2011**, *26*, 271–273.
30. Mohammadi, A.; Khakzad, A.; Rashidnejad Omran, N.; Mahvi, M.R.; Moarefvand, P.; Afzal, P. Application of number-size(N-S) fractal model for separation of mineralized zones in Dareh-Ashki gold deposit, Muteh Complex, Central Iran. *Arab. J. Geosci.* **2013**, *6*, 4387–4398.
31. Cheng, Q.; Li, Q. A fractal concentration-area method for assigning a color palette for image representation. *Comput. Geosci.* **2002**, *28*, 567–575.
32. Shahriari, H.; Ranjbar, H.; Honarmand, M. Image segmentation for hydrothermal alteration mapping using PCA and concentration-area fractal model. *Nat. Resour. Res.* **2013**, *22*, 191–206.
33. Asl, R.A.; Afzal, P.; Adib, A.; Yasrebi, A.B. Application of multifractal modeling for the identification of alteration zones and major faults based on ETM+ multispectral data. *Arab. J. Geosci.* **2015**, *8*, 2997–3006.
34. Zhang, X.; Zhang, H. Geochronological, geochemical, and Sr–Nd–Hf isotopic studies of the Baiyanghe A-type granite porphyry in the Western Junggar: Implications for its petrogenesis and tectonic setting. *Gondwana Res.* **2014**, *25*, 1554–1569.

35. Xiao, Y.D.; Huang, J.H.; Wang, Z.; Wang, S.C.; Zhou, Y.B.; Li, Q.D. Spatial distribution of uranium and beryllium ore bodies in the Baiyanghe deposit, Hebukesai county, Xiangjiang. *West-China Explor. Eng.* **2011**, *9*, 123–126. (In Chinese)
36. Xiao, Y.D. Study on Genesis of Baiyanghe Uranium-Beryllium Deposit in Hebukeser, Xinjiang. Master's Thesis, Xinjiang University, Urumqi, Xinjiang, China, 2011. (In Chinese)
37. Mao W.; Wang, G.; Li, X.F.; Wang, M.; Xiao, R. A study of fluid inclusions in Baiyanghe U-Be deposit, Xinjiang. *Miner. Depos.* **2013**, *32*, 1026–1034. (In Chinese)
38. Yang, W.L.; Mostafa, F.; Li, Y.L.; Wang, M.; Zhou, J. Characteristics of fluorite and fluid inclusions in the Baiyanghe U-Be deposit, west Junggar. *Xinjiang Geol.* **2014**, *32*, 82–86. (In Chinese)
39. Zhang, X.; Zhang, H. Geochemical characteristics of the ore-forming fluid and ore genesis of the Baiyanghe Be-U deposit, Xinjiang, China. *Geochimica* **2013**, *42*, 143–152. (In Chinese)
40. Xiu, X.Q.; Fan, H.H.; Ma, H.F.; Yi, L.S. The wall rock alteration and its geochemical characteristics of Baiyanghe uranium and beryllium deposit, Xinjiang. *Uranium Geol.* **2011**, *27*, 215–220 (In Chinese)
41. Sadeghi, B.; Khalajmasoumi, M.; Afzal, P.; Moarefvand, P.; Yaserbi, A.B.; Wetherelt, A.; Foster, P.; Ziazarifi, A. Using ETM+ and ASTER sensors to identify iron occurrences in the Esfordi 1:100,000 mapping sheet of Central Iran. *J. Afr. Earth Sci.* **2013**, *85*, 103–114.

© 2015 by the authors; licensee MDPI, Basel, Switzerland. This article is an open access article distributed under the terms and conditions of the Creative Commons Attribution license (<http://creativecommons.org/licenses/by/4.0/>).